Published in final edited form as:

Nat Struct Mol Biol. 2017 November ; 24(11): 965–976. doi:10.1038/nsmb.3482.

Architectural alterations of the fission yeast genome during the cell cycle

Hideki Tanizawa, **Kyoung-Dong Kim**, **Osamu Iwasaki**, and **Ken-ichi Noma**

The Wistar Institute, Philadelphia, Pennsylvania, USA

Abstract

Eukaryotic genomes are highly ordered through various mechanisms, including topologically associating domain (TAD) organization. We employed an *in situ* Hi-C approach to follow the 3D organization of the fission yeast genome during the cell cycle. We demonstrate that during mitosis, large domains of 300 kb–1 Mb are formed by condensin. This mitotic domain organization does not suddenly dissolve, but gradually diminishes until the next mitosis. By contrast, small domains of 30–40 kb that are formed by cohesin are relatively stable across the cell cycle. Condensin and cohesin mediate long-and short-range contacts, respectively, by bridging their binding sites, thereby forming the large and small domains. These domains are inversely regulated during the cell cycle but assemble independently. Our study describes the chromosomal oscillation between the formation and decay phases of the large and small domains, and we predict that the condensin-mediated domains serve as chromosomal compaction units.

Recently developed genomic approaches, such as genome-wide chromosome conformation capture (Hi-C) and chromatin interaction analysis by paired-end tag sequencing (ChIA-PET), have been applied to various organisms[1–3]. Rapidly accumulating studies have offered comprehensive insights into enhancer-promoter interactomes[4–6] and, importantly, identified a new layer of genome organization: TAD formation[7–10]. TADs represent functional genome-organizing units, linked to coregulating transcription, organizing euchromatin and heterochromatin domains, and coordinating replication timing[8,11,12]. At this early stage of research associated with TADs and other types of topological domains, many important questions remain unresolved; for example, how topological domains of different sizes are formed and regulated during the cell cycle in distinct organisms remains largely unclear. Currently available data suggest that mammalian TADs diminish during mitosis and reappear during the G1 phase[13–15].

Correspondence to should be addressed to K.N. (noma@wistar.org).

AUTHOR CONTRIBUTIONS

H.T. performed the *in situ* Hi-C experiments and bioinformatics analyses. K.K. performed the ChIP, FISH and RNA-seq experiments. O.I. performed the FISH experiments. K.N. conceived and designed the study. All authors contributed to the data analyses and the writing of the manuscript.

COMPETING FINANCIAL INTERESTS

The authors declare no competing financial interests.

For many years, it has been appreciated that the activities of mitotic chromosome assembly and sister-chromatid cohesion are mediated by the SMC (structural maintenance of chromosomes) complexes condensin and cohesin[16–18]. Condensin is implicated in large-scale genome organizing events, including topological domain formation and chromosome territory arrangement[19–23]. Cohesin is involved in TAD formation in addition to promoter–enhancer looping[4,24]. How condensin and cohesin mediate the organization of TADs and other types of topological domains, which can potentially affect each other, remains enigmatic. Here, we describe how condensin and cohesin organize the 3D genome architecture, especially topological domains, during the cell cycle.

RESULTS

Oscillation of chromosomal architecture during the cell cycle

We optimized the *in situ* Hi-C procedure[25] for fission yeast cells (Supplementary Fig. 1) and found that this method was highly reproducible and 2–3 times more efficient at recovering sequence reads reflecting physical proximity between DNA sections compared to standard Hi-C (Supplementary Table 1, Supplementary Fig. 2 and Supplementary Note 1). To understand how the genomic architecture is regulated across the cell cycle, we applied the *in situ* Hi-C procedure to cell-cycle-synchronized fission yeast cells. Using the *cdc25-22* mutant, the cell cycle was synchronized for more than 95% of cells (Supplementary Fig. 2f). Cells harvested at 10-min intervals were subjected to *in situ* Hi-C experiments, and eight genome-wide contact maps were generated throughout the cell cycle (Fig. 1a and Supplementary Fig. 3a). The 60–70 million paired reads obtained for the respective time points resulted in a 4–8-kb resolution (Supplementary Tables 1 and 2). The highest resolutions were defined as previously described[26]. Local contacts, represented as diagonal lines, were prominent at all times, whereas interchromosomal and intrachromosomal contacts appeared to vary in a cell-cycle-dependent manner (Supplementary Fig. 3a). For instance, read numbers reflecting interchromosomal contacts were significantly different between interphase and mitosis ($P = 0.0042$, two-sided Student's t test) (Fig. 1b). Interchromosomal contacts were relatively more frequent during interphase between the 70- and 120-min time points (G1/S–G2), whereas intrachromosomal contacts occurred with greater frequency during M phase between the 30- and 50-min points (mid M–M/G1).

Further analysis of intrachromosomal contacts revealed that the frequencies of long-range contacts in the 75 kb–1 Mb range were sequentially enhanced over the 20- to 40-min points as cells progressed through mitosis (Fig. 1c, top). In contrast, the long-range contacts gradually decreased over the 50- to 120-min points as cells exited mitosis and progressed through interphase (Fig. 1c, bottom). Plotting the average contact scores against distance revealed that the slope of distance-dependent decay changed around 280 kb at the 30-min point (mid M), suggesting that contact scores within 280 kb decrease less rapidly against distance than those beyond 280 kb (Supplementary Fig. 3b). Moreover, around 400 and 500 kb became transition points at the 40- and 50-min points (mid M and M/G1), respectively. These results suggest that genomic loci tend be in contact in larger areas as cells progress through mitosis.

To investigate in more detail how intrachromosomal contacts are modulated during the cell cycle, we calculated the difference and $\log_2$ ratio of contact scores between two consecutive time points (Fig. 1d,e and Supplementary Fig. 4). We observed that intrachromosomal contacts in the 75 kb–1 Mb range were promoted at the 120–20-min, 20–30-min, and 30–40-min transitions (G2–mid M) when the contacts <75 kb and >1 Mb were reduced (Fig. 1e). Subsequently, the intrachromosomal contacts in the 75 kb–1 Mb range were continuously reduced in the following interphase, whereas the other contacts were promoted (Fig. 1e). It should be noted that, as cells progressed through mitosis, the intrachromosomal contacts encroached on larger areas; peaks of genomic distances with the enhanced intrachromosomal contacts were 250, 500, and 800 kb at the 120–20-min, 20–30-min, and 30–40-min transitions, respectively, thus suggesting that chromosomes are gradually compacted during mitosis.

We visualized the two loci separated by 400 kb using fluorescent *in situ* hybridization (FISH) (Fig. 1f, top). The distance between the two loci became relatively shorter between the 30- and 50-min points (mitosis) than during interphase ($P = 0.00104$, two-sided Mann–Whitney U test). To compare FISH data with the *in situ* Hi-C data, we estimated physical distances between every two loci separated by 400 kb during the cell cycle (Fig. 1f, bottom). FISH data were correlated with the genomic data when median distances from FISH and *in situ* Hi-C data were compared (Pearson's correlation $r = 0.702$). These results collectively suggest that the 75 kb–1 Mb long-range contacts are regulated during the cell cycle and that the oscillation between the processes of chromosomal condensation and decondensation stretches throughout the cell cycle. Additionally, we found that centromeric and telomeric contacts are both regulated during the cell cycle (Supplementary Fig. 5 and Supplementary Note 1).

Modulation of large topological domains during the cell cycle

We detected 300 kb–1 Mb chromatin domains and observed that these domains became clearer between the 20- and 50-min time points (M phase) than during the following interphase (Fig. 2a and Supplementary Fig. 6). The domain organization was most evident at the 40-min point (mid M), suggesting that this organization is likely linked to mitotic chromosome assembly. We recognized that this domain organization was clearer on the long arms of chromosomes I and II, where we observed two domain borders on the left arm of chromosome I and one border on the right arm of chromosome II (Fig. 2a and Supplementary Fig. 6b). Interestingly, we observed that the domain was enlarged around 100 kb between the 30- and 40-min time points (mid M), implying that the enlargement results from chromatin-loop extrusion (Fig. 2a; see Discussion). It is also important to note that the large domains overlapped the weaker domains (Supplementary Fig. 6). We hypothesize that the domains are probably organized in different cells.

To further analyze how the domains are modulated during the cell cycle, we examined the difference of intrachromosomal contact scores between two consecutive time points and observed that the domain organization was promoted between the 120- and 40-min time points (G2–mid M) and gradually diminished in the subsequent time points (Supplementary Fig. 7a).

Because the 40- and 120-min points (mid M and G2) showed the strongest and weakest (or no) large domains, respectively, we compared contact scores between these two time points. Using the variation between the biological replicas (120-min point), we defined significantly up- and downregulated genomic contacts at the 40-min point compared to the 120-min point (false discovery rate (FDR) < 0.005, two-sided paired Student's *t* test; Fig. 2b). We observed that the upregulated contacts were derived from the 75 kb–1 Mb range, whereas the downregulated contacts were derived from either the <75-kb or >1-Mb ranges (Supplementary Fig. 7b,c). The downregulated far-range contacts (>1 Mb) consisted of interarm and interchromosomal contacts as well as centromeric and telomeric contacts, suggesting that the Rabl-like chromosomal configuration is impaired during mitosis (Supplementary Fig. 7b). Note that those significantly altered contacts were hardly detected between other biological replicas from the 60-min points (Supplementary Fig. 7d). The upregulated contacts were often positioned within the large domains that were observed at the 40-min time point (Supplementary Fig. 7e) and in the comparison maps showing subtraction and $\log_2$ ratios of contact scores between the 40- and 120-min points (Fig. 2c). We observed that the frequency for large-domain interactions of significantly upregulated contacts was significantly higher than the distance-conserved random distribution ($P = 1.13 \times 10^{-107}$, one-sided Student's *t* test; Supplementary Fig. 7f).

To investigate how contacts within the large domains are controlled during the cell cycle, we calculated $\log_2$ ratios of contact scores between two consecutive time points for genomic contacts within the large domains and observed that these were promoted at the 120–20-min, 20–30-min and 30–40-min transitions between G2–mid M, whereas they were reduced after the 50-min point during inter-phase (Fig. 2d).

To further examine how the large domains contribute to *in vivo* chromosome assembly, we performed FISH analysis during the cell cycle (Fig. 2e). We observed that at the 30- and 40-min time points, the two gene loci present within the same domain (L2) were positioned significantly closer compared to the loci spanning the two domains (L1) ($P < 0.0001$, two-sided Mann–Whitney *U* test). Moreover, median distances of the L1 and L2 paired loci were significantly different during the cell cycle ($P = 0.0173$, two-sided Student's *t* test). These results show that the large domains serve as endogenous units reflecting mitotic chromosome organization and compaction. Furthermore, we compared the FISH data with the *in situ* Hi-C data from different cell-cycle stages. Every genomic combination separated by 400 kb was divided into two categories, one in which the two loci are positioned within the large domains and the other in which the two loci are between the large domains, and contact scores were converted to physical distances (Fig. 2f), as explained in Figure 1f. Median distances between loci within the large domains were significantly different than those between the large domains ($P = 2.25 \times 10^{-6}$, two-sided Student's *t* test), strongly suggesting that the large domains defined in this study reflect the endogenous genome-organizing units. We observed that FISH data for the L2 were well correlated with the genomic data when we compared the median distances estimated from FISH and *in situ* Hi-C data within the large domains (Pearson's correlation $r = 0.814$). Together, these results suggest that the large domains are the *in vivo* chromosomal architecture, which is promoted during mitosis and gradually diminishes during interphase.

Inverse correlation between small- and large-domain organizations during the cell cycle

It has been shown that the fission yeast genome is organized into ~50-kb domains, hereby referred to as small domains[21,27]. The *in situ* Hi-C approach detected the presence of these small domains consistently during the cell cycle (Fig. 3a,b). The average domain size was around 30–40 kb throughout the cell cycle (Fig. 3b).

Although the small domains exist during the cell cycle, it is possible that they are regulated in a cell-cycle-dependent manner. Indeed, the significantly downregulated contacts at the 40-min time point (mid M) compared to those of the 120-min time point (G2) were more often positioned within the small domains (Supplementary Fig. 7g). The frequency of small-domain interactions in the downregulated contacts was significantly higher than the distance-conserved random distribution ($P = 2.61 \times 10^{-113}$, one-sided Student's *t* test; Supplementary Fig. 7h). We further observed that contact scores within the small domains were slightly reduced at the 20–30-min and 30–40-min transitions between G2/M and mid M (Fig. 3c) when the large domains were enhanced. Medians of $\log_2$ ratios between contact scores within the large and small domains were negatively correlated during the cell cycle (Pearson's correlation $r = -0.676$; Figs. 2d and 3c). These data indicate that the organizations of the large and small domains are inversely regulated during the cell cycle.

We observed that the significantly up- and downregulated contacts observed between the 40- and 120-min time points were positioned in the 75–800 kb and <75 kb ranges, respectively (Supplementary Fig. 7i,j). We further dissected these altered contacts into different cell-cycle stages and observed that the significantly altered contacts in the 75–800 kb range were upregulated between the 120- and 40-min points (G2–mid M) and downregulated after the 50-min point during interphase (Supplementary Fig. 7k). The significantly altered contacts in the <75-kb range were downregulated between the 120- and 40-min points (mitosis) and upregulated between the 50- to 120-min points (M/G1–G2) (Supplementary Fig. 7k). Taken together, these results suggest that 75–800-kb genomic contacts mediate the 300 kb–1 Mb large-domain organization and that <75-kb contacts mediate the 30–40-kb small-domain organization. Note that the neighboring small domains were often merged into joint domains (Fig. 3a). Therefore, the small-domain organization can be explained by <75-kb contacts.

Moreover, we compared contact scores at different time points and observed that contact scores in the <75-kb and >1-Mb ranges exhibited good correlation across the cell cycle, whereas there was less correlation were in the 75 kb–1 Mb range between the different cell-cycle stages, especially between mitosis and interphase (Fig. 3d). Because the 75 kb–1 Mb range accounts for the large-domain organization, this domain organization is a major contributor to the cell-cycle-dependent architectural alteration, whereas the small domains are relatively stable and exist across the cell cycle.

Condensin-dependent large-domain organization

Because the organization of 300 kb–1 Mb large domains is promoted during mitosis, we hypothesized that the large domains are formed by condensin. To address this premise, we performed *in situ* Hi-C with the *cut14-208* and *cut3-477* condensin mutants. Because these mutant cells were cultured at 36 °C, we examined the effects of 36 °C culture on genome-

wide contacts. Interestingly, we observed that the 36 °C culture affected the large- and small-domain organization (Supplementary Fig. 8a–f and Supplementary Note 1). We obtained *in situ* Hi-C matrices in the *cut14-208* and *cut3-477* condensin mutants (Fig. 4a and Supplementary Fig. 8g). Contact scores decreased more rapidly in the condensin mutants than in the wild-type cells (WT1 and WT2), and they were reduced by around 75–800 kb in the *cut14-208* and *cut3-477* mutants compared to the WT1 and WT2, respectively, suggesting that condensin mediates contacts in the 75–800-kb range (Fig. 4b,c and Supplementary Fig. 8h,i).

To further examine whether the condensin mutations disrupt the organization of the large domains, we generated difference maps between the wild type and condensin mutants and observed that the large domains receded in the condensin mutants (Fig. 4d,e and Supplementary Fig. 8jk,). The receding domains were consistent with the large domains detected at the 40-min time point (mid M) (Fig. 4f and Supplementary Fig. 8k, bottom). Contact scores in the large domains were significantly affected by the condensin mutations ($P = 6.82 \times 10^{-10}$ and 1.23×10^{-6} for *cut14-208* and *cut3-477*, respectively, two-sided paired Student's *t* test; Fig. 4g and Supplementary Fig. 8l). We also compared $\log_2$ ratios of contact scores within the large domains between the *cut14-208* and WT1 and between the WT2 and WT1 and observed that contact scores in the *cut14-208* were significantly different from those of WT2 ($P = 6.37 \times 10^{-4}$, two-sided paired Student's *t* test), indicating that the effect of the condensin mutation on large-domain organization is significantly more severe than the effect of 36 °C culture (Supplementary Fig. 8m). These data indicate that condensin contributes to contacts in the large domains.

Cohesin-mediated small-domain organization

It has previously been suggested that cohesin is required for the formation of ~50-kb domains[21,27]. We posited that these domains are identical to the stable small domains detected by the *in situ* Hi-C study (Fig. 3a). We applied the *in situ* Hi-C approach to the *rad21-K1* cohesin mutant (Fig. 4h) and compared contact scores between the *rad21-K1* mutant and WT2, both of which were cultured at 36 °C for 2 h (Fig. 4i). We observed that the slope of distance-dependent decay was changed at the 75-kb point in the wild type, whereas this transition point disappeared in the *rad21-K1* mutant, implying that short-range contacts within 75 kb became less frequent in the mutant (Fig. 4j). When we compared the contact maps between the *rad21-K1* mutant and WT2 (Fig. 4k), we observed that contacts in the small domains were reduced in the cohesin mutant (Fig. 4l). Because two neighboring small domains are often merged, as described above (Fig. 3a), the difference map indicated that reduced contacts were also detected in the merged domains (Fig. 4l). Contact scores in the small domains were significantly impaired by the *rad21-K1* mutation ($P = 1.75 \times 10^{-20}$, two-sided paired Student's *t* test; Fig. 4m). These results indicate that cohesin mediates contacts in the small domains.

Involvement of condensin- and cohesin-binding sites in long- and short-range contacts

We hypothesized that condensin mediates long-range contacts and cohesin mediates short-range contacts, thereby forming the large and small topological domains, respectively. To test this hypothesis, we examined how condensin- and cohesin-binding sites are connected

throughout the genome. We noticed that condensin- but not cohesin-binding sites were less efficiently recovered by the *in situ* Hi-C experiments compared to other loci (Fig. 5a). The DNA amounts of condensin-binding sites were significantly different from the distribution of every locus ($P = 6.93 \times 10^{-20}$ and 0.0322 for condensin and cohesin sites, respectively, two-sided Mann-Whitney U test). We speculated that condensin might be a part of the insoluble nuclear architecture, as predicted in previous reports[28,29], and mediates gene contacts, thereby slightly reducing the efficiency of DNA extraction when loci are bound by condensin. Therefore, we normalized the contact maps based on DNA amounts estimated from read numbers of self-ligation and undigested products (Fig. 5b).

We observed that contacts between condensin-binding sites positioned >75 kb apart were enhanced between the 20- and 50-min time points (mitosis) compared to those of the *cut14-208* condensin mutant (Fig. 5c, top). In contrast, contacts between cohesin-binding sites within 75 kb were increased across the cell cycle compared to those of the *rad21-K1* cohesin mutant (Fig. 5c, bottom). Contact scores between condensin-binding sites in the 75 kb–1Mb range were significantly higher than those in the condensin mutant during mitosis (Fig. 5d). Contact scores between cohesin-binding sites in the <75-kb range were significantly higher than those in the cohesin mutant across the cell cycle (Fig. 5d).

To further connect condensin and cohesin binding to distance-dependent genomic contacts, we compared the binding strengths of condensin and cohesin to contact scores. Every locus was ranked by condensin and cohesin enrichment, and we found that strong condensin-binding sites tend to mediate long-range contacts (75 kb–1Mb). For instance, condensin binding strength and average contact scores in the 75 kb–1 Mb range were well correlated throughout mitosis (Pearson's correlation $r = 0.82$, 0.76, 0.82, and 0.79 for the 20-, 30-, 40-, and 50-min time points, respectively; Fig. 5e). On the other hand, strong cohesin-binding sites participated in short-range contacts within 75 kb during the cell cycle. Cohesin-binding scores and average contact scores in the <75-kb range were well correlated throughout the cell cycle (Pearson's correlation $r = 0.73$–0.92; Fig. 5f).

Furthermore, immunofluorescence and ChIP results revealed that the nuclear localization of condensin and its enrichment at target loci were promoted during mitosis, whereas nuclear localization of cohesin and its binding to target loci were stable across the cell cycle (Supplementary Figs. 9 and 10 and Supplementary Note 1). These results collectively suggest that the nuclear localization of condensin and cohesin promotes their chromatin binding and that condensin and cohesin bridge their binding sites to preferentially mediate 75 kb–1 Mb long-range contacts during mitosis and <75 kb short-range contacts throughout the cell cycle, respectively.

Contexts of condensin- and cohesin-mediated contacts

To further investigate how condensin- and cohesin-mediated contacts contribute to the organization of the large and small domains, we compared the *in situ* Hi-C data to the condensin and cohesin ChIA-PET data[21]. We found that the large domains were consistently observed in the *in situ* Hi-C map from the 40-min time point (mitosis), the difference map between the *cut14-208* and WT1, and the condensin ChIA-PET map (Fig. 6a). Condensin-mediated contacts predicted from the ChIA-PET data were preferentially positioned within

the large domains (Fig. 6a). For instance, when we plotted averages and $\log_2$ ratios of contact scores between the 40- and 120-min points and highlighted genomic contacts within the large domains and those that overlapped with condensin-mediated contacts predicted from the ChIA-PET data, the distributions of scores showed similar patterns, thus implying that condensin-mediated contacts are preferentially present within the large domains (Fig. 6b). Indeed, we observed that the frequency of large-domain interactions within the condensin-mediated contacts predicted from the ChIA-PET data was significantly higher than the distance-conserved random distribution ($P = 4.18 \times 10^{-30}$, one-sided Student's *t* test; Fig. 6c).

Cohesin-mediated contacts were predicted from the cohesin ChIA-PET data, and they were often positioned within the small domains that were detected in both the *in situ* Hi-C map (120-min point) and the difference map between *rad21-K1* and WT2 (Fig. 6d). For instance, we observed that the distributions of scores within the small domains and from cohesin-mediated contacts predicted from the ChIA-PET data showed similar patterns (Fig. 6e). The frequency for the small-domain interactions within the cohesin-mediated contacts from the ChIA-PET data was significantly higher than the distance-conserved random distribution ($P = 1.39 \times 10^{-44}$, one-sided Student's *t* test; Fig. 6f). These results further support our notion that condensin and cohesin bind to genomic regions to mediate long- and short-range contacts within the large and small domains, respectively.

Independence between condensin- and cohesin-mediated domain organizations

We observed that condensin and cohesin mediate large- and small-domain organization, respectively, which are inversely correlated during the cell cycle (Pearson's correlation $r = -0.676$; Figs. 2d and 3c). Therefore, it is possible that the condensin- and cohesin-mediated domain organizations potentially play an inhibitory role to each other. To test this possibility, we compared the contact maps in the *cut14-208* condensin mutant and WT1 and observed that contacts in the small domains were not preferentially promoted in the condensin mutant (Fig. 7a). Contact scores in the small domains were marginally affected by the condensin mutation ($P = 0.005$, two-sided paired Student's *t* test; Fig. 7b) compared to the effect of the *rad21-K1* cohesin mutation on contact scores within the small domains ($P = 1.75 \times 10^{-20}$, two-sided paired Student's *t* test; Fig. 4m). Therefore, we predict that the condensin mutation does not specifically facilitate contacts in the small domains (Fig. 7a, top).

Moreover, we observed that the *rad21-K1* cohesin mutation did not promote large-domain organization (Fig. 7c). Contact scores in the large domains were scarcely affected by the cohesin mutation ($P = 0.0364$, two-sided paired Student's *t* test; Fig. 7d) compared to the effects of the condensin mutations on contact scores within the large domains ($P = 6.82 \times 10^{-10}$ and 1.23×10^{-6} for the *cut14-208* and *cut3-477* mutants, two-sided paired Student's *t* test; Fig. 4g and Supplementary Fig. 8l). It is unlikely that the cohesin mutation particularly enhances contacts in the large domains (Fig. 7c).

We also performed the *in situ* Hi-C using the *cut3-477 rad21-K1* condensin–cohesin double mutant, referred to as DM. The difference map between the DM and *rad21-K1* single mutant indicated that the large domains were impaired in the DM compared to those of the *rad21-K1*, suggesting that the large domains are preserved in the cohesin mutant (Fig. 7e).

Consistently, contact scores in the large domains were significantly different between the DM and *rad21-K1* mutant ($P = 7.86 \times 10^{-7}$, two-sided paired Student's *t* test; Fig. 7f).

We also compared the DM with the *cut3-477* condensin single mutant (Fig. 7g). The difference map between the DM and condensin mutant exhibited reduction in the small domains, implying that the small domains exist in the condensin mutant (Fig. 7g). Therefore, contact scores in the small domains were significantly different between the DM and *cut3-477* mutant ($P = 7.52 \times 10^{-20}$, two-sided paired Student's *t* test; Fig. 7h). All together, these results demonstrate that condensin and cohesin independently organize the large and small domains, respectively, although they are inversely correlated during the cell cycle.

Although how condensin-mediated genome organization impacts transcriptional regulation is not fully understood, our RNA-seq analyses revealed that condensin or its mediated genome organization participates in maintaining the expression of subtelomeric genes (Supplementary Table 3, Supplementary Fig. 11 and Supplementary Note 1).

DISCUSSION

It is known that the Rabl-like chromosomal configuration exists during interphase in yeasts and flies[19,30–32]. This study indicates that centromeres and telomeres respectively cluster during interphase, suggesting the Rabl-like configuration in fission yeast. During mitosis, when chromosomes are subjected to condensin-dependent domain organization and compaction, centromeric and telomeric contacts as well as interarm and interchromosomal contacts diminish. As inter-phase progresses, the condensin-mediated chromosomal organization gradually degrades, and chromosomal arm regions become flexible and are able to associate with other arms in the same or different chromosomes, thereby allowing for the Rabl-like configuration of chromosomes (Fig. 7i, top).

Cohesin has been implicated in TAD organization[6,24,33,34]. This study shows that cohesin-dependent small domains, fission yeast TADs, exist throughout the cell cycle, probably because cohesin localizes in the nucleus and binds to its target loci throughout the cell cycle. When the organization of the condensin-mediated larger domains is promoted during mitosis, the cohesin-mediated small domains become impaired. Although the organization of the condensin and cohesin domains is negatively correlated during the cell cycle, they are assembled independently of each other.

Condensin is implicated in domain organization in fission yeast and other eukaryotes[20,21,23]. Our *in situ* Hi-C data in the fission yeast system reveal that condensin mediates the organization of the 300 kb–1 Mb large domains and that those large domains are formed during mitosis and gradually degrade during the following phases. The mitotic domains formed by condensin have also been detected in recent Hi-C and ChIA-PET studies[21,35]. It has been suggested that human chromosomes are devoid of topological domains, including TADs and larger domains, such as compartments A and B, during mitosis[13,15]. Moreover, a recent study suggests that mammalian TADs gradually become weaker as cells progress through interphase[15], which was not observed in fission yeast. The collective results from

these studies imply that the cell-cycle-dependent regulation of topological domains is likely different among species.

Our studies demonstrate that condensin-binding sites are interconnected within the large domains[21]. Currently, two models have been proposed to explain the formation of topological domains: loop-extrusion and transient-contact models. In the loop-extrusion model, looping molecules, such as cohesin or condensin, are recruited to gene loci, and chromatin loops are extruded from the looping molecules until they reach adjoining loops, thereby resulting in the generation of consecutive domains[36–38]. The transient-contact model explains that dynamic binary contacts mediated by condensin are sufficient to generate topological domains[39]. We observed that the condensin-mediated contact domain extends during mitosis as the cell cycle progresses (Fig. 2a), implying that the loop bridging the two borders encroaches on the neighboring region via the loop extrusion.

Condensin is required for mitotic chromosome organization, and its absence leads to the formation of chromosomal bridges during ana-phase[40–42]. This study predicts that condensin mediates the formation of the large domains during mitosis, and this domain organization and gene contacts within the domains cause chromosomal compaction and potentially make chromatin fibers rigid, thus facilitating the transmittal of physical force pulling the kinetochore to chromosomal arms, thereby improving the fidelity of chromosomal segregation (Fig. 7i, bottom)[43].

ONLINE METHODS

Strains and culture conditions

Cut14 (condensin) and Rad21 (cohesin) proteins were tagged with Myc or Pk at the C termini of their proteins using a PCR-based module method[45,46]. Tagged proteins were expressed from their endogenous gene loci with their own promoters. Strain constructions were performed using conventional genetic crosses. The fission yeast *Schizosaccharomyces pombe* strains (Supplementary Table 4) were cultured in Yeast-Extract Adenine (YEA).

Cell-cycle synchronization

The *cdc25-22* mutant was used for the cell-cycle synchronization as previously described[47]. Exponentially growing cells were cultured at 26 °C in YEA medium until the O.D. reached 0.25 and subsequently incubated at 36 °C for 3.5 h. The cell cycle was efficiently arrested at the G2–M transition and released by further culturing the cells at 26 °C. After the release, the cells were harvested at the indicated time points.

Fission yeast *in situ* Hi-C

The *in situ* Hi-C experiment was performed as previously reported[25] with modifications (Supplementary Fig. 1a). Briefly, 15×10^8 fission yeast cells were fixed with 3% paraformaldehyde at 26 °C for 15 min. Fixed cells were disrupted using the bead beater (Biospec products) in the presence of complete protease inhibitor cocktail (Roche). Cell lysate was incubated at 62 °C for 7 min in 0.625% SDS solution and subsequently with 1% Triton-X 100. DNA was digested with 50 units of MboI at 37 °C overnight. After

centrifugation (3,000 r.p.m. for 10 min), the pellet was used in the following procedure. Restriction fragments were filled in with 150 μM biotin-14-dATP, dCTP, dGTP, and dTTP using 40 units of Klenow fragment at 37 °C for 45 min, then subjected to proximity ligation using 2,000 cohesive end units of T4 DNA ligase (NEB) at 26 °C for 4 h in 1 ml volume with gentle rotation. DNA was reverse crosslinked at 68 °C overnight in the presence of 0.4 M NaCl and proteinase K and purified by phenol/chloroform extraction. Purified DNA was sheared by the Bioruptor (Diagenode) to obtain a size range of 100–500 bp. Biotin-labeled DNA was purified using Dynabeads (MyOne Streptavidin C1, Thermo Fisher Scientific). Sequencing adapters were ligated using the NEBNext Multiplex Oligos for Illumina kit while DNA was attached to the beads. DNA was then eluted by incubating the beads at 90 °C for 10 min, then PCR amplified using the NEBNext Q5 Hot Start HiFi PCR master Mix. PCR products were sequenced on the Illumina HiSeq 2000 platform to obtain 76-bp paired-end reads.

Data processing of *in situ* Hi-C

Sequence alignment—The 76-bp paired reads were separately aligned to the fission yeast genome (version ASM294v2.19) using Bowtie2 (v2.2.9) (ref. 48). Partial alignment was judged using the CIGAR string. Unaligned bases were trimmed, and a remaining sequence was realigned. If alignable locations were not identified across the genome, either upstream or downstream, five bases were trimmed. Reads were again evaluated using the CIGAR string, and the trimming step was repeated until the truncated reads became less than 25 bp. Mapped reads were assigned to MboI fragments.

Filtering processes—As shown in Supplementary Figure 1b, redundant paired reads mapped to the same exact genomic positions were discarded to remove a potential PCR bias. When reads were aligned to repetitive sequences or had low mapping quality (MapQ < 30), they were also removed. Subsequently, paired reads aligned to two loci positioned <20 kb apart and potentially derived from self-ligation and undigested products were discarded. Self-ligation and undigested products are further discussed in the next section. Read numbers that remained after the filtering processes are detailed in Supplementary Table 1.

Self-ligation and undigested products—Self-ligation connects both ends of linear DNA molecules without reflecting gene contacts. Among the possible ligations, only the ‘out-out’ combination can be explained by a self-ligation event (Supplementary Fig. 1b). Paired reads showing the ‘in-in’ context are potentially derived from undigested products. Read numbers from self-ligation and undigested events were counted and summarized in Supplementary Figure 2a (Supplementary Table 1). To eliminate the effects from self-ligation and undigested products, the total read number ($z + w$) solely reflecting gene contacts was predicted as the sum of x and y (Supplementary Fig. 1b).

Contact maps—For the raw contact map, contact matrices were generated at three resolutions, such as 5, 10, and 20 kb. Note that 5- and 10-kb resolutions were used for analyzing the small and large topological domains, and that 20-kb resolution was employed to show the entire *in situ* Hi-C maps. The entire fission yeast genome was divided into 5-,

10-, or 20-kb sections. A raw contact matrix was first constructed by counting paired reads assigned to two genomic sections. Reads belong to MboI fragments.

For bias correction, biases in raw contact matrices were corrected using the ICE method[49]. The ICE normalization was repeated ten times, because *in situ* Hi-C matrix biases were no longer reduced after ten iterations (Supplementary Fig. 1c). An average score of the bias-corrected contact matrix was adjusted to 1, resulting in contact scores.

Comparison of two contact maps—Comparison maps shown in this study represent subtraction scores or $\log_2$ ratios of contact scores.

Border strength

Border strength was determined as previously described[21,50]. The fission yeast genome was divided into 5- and 10-kb bins for small- and large-domain analyses, respectively. To calculate the border strength at a specific bin, total intradomain contacts within upstream and downstream 5 and 20 bins were calculated for small and large domains, respectively. Contact scores were used for this calculation. Additionally, total interdomain contacts between upstream and downstream 5 and 20 bins were estimated for small and large domains, respectively. The ratios between intra- and interdomain contacts were calculated for every bin, and the average ratio was subtracted from the respective ratios. These values were then divided by the s.d., resulting in border strength scores. A high border-strength score indicates that intradomain contacts within upstream and downstream domains are more frequent than interdomain contacts between upstream and downstream domains, thereby implying a potential existence of domain border. Genomic positions showing positive border-strength scores were defined as domain borders.

Detection of significantly altered contacts

Averages and $\log_2$ ratios of contact scores were calculated between the biological replicates (120-min time point) and between paired targets of *in situ* Hi-C data. The biological replicates were derived from two independent *in situ* Hi-C experiments using independent cultures. In the experiments presented in Figure 2b, paired targets are from the 40- and 120-min data. Note that every combination (n = 787,512) of DNA sections (10-kb bins) was subjected to this analysis. Significantly up- (red) and down- (blue) regulated genomic contacts were defined by FDR < 0.005 and calculated as follows: based on average contact scores between the biological replicates, genomic contacts were categorized into 20 groups in which the respective groups have at least 5,000 contacts. Next, based on an average contact score between the paired targets (40- and 120-min data in Figure 2b), a combination of two genomic loci was assigned to the specific group in the biological replicate data. Genomic contacts were randomly selected from the assigned group for 10,000 times, and the distribution of $\log_2$ ratios of contact scores between the biological replicates was used for calculation of the P value, which estimates the significance of the $\log_2$ ratio of contact scores between the paired targets. Every combination was subjected to this P value calculation. The FDR was calculated for each of the P values using the Benjamini–Hochberg method[51]. The FDR was set as < 0.005 unless otherwise noted.

DNA-amount normalization of contact scores

Self-ligation and undigested products were defined as described above. DNA amount for a specific bin (5 kb) was estimated as the number of reads derived from self-ligation and undigested products, and this estimation was subjected to every bin. A raw contact score between two bins (A and B sections) was estimated as the number of reads assigned to the combination, and the raw score was divided by DNA amounts estimated for A and B sections. This DNA-amount normalization was applied to every combination. An average score of DNA-amount-normalized matrix was adjusted to 1, resulting in DNA-amount-normalized contact scores (used for Fig. 5b–d).

DNA-amount-normalized contact scores were further subjected to distance normalization (used for Fig. 5e,f). Average contact scores between every two loci (5-kb bins) separated by same distances were calculated. Contact scores in the DNA-amount-normalized Hi-C matrix were divided by average contact scores with the same distances. Note that DNA-amount-normalized and distance-normalized contact scores were only employed for the analyses described in Figure 5.

Comparison between condensin and cohesin binding and distance-dependent contacts

The fission yeast genome, except centromeres and telomeres, was divided to 5-kb bins, and condensin- and cohesin- binding strength to respective bins were estimated based on enrichment of condensin and cohesin, respectively[21]. The gene loci (5-kb bins) were classified into 19 groups, and the respective groups were ordered from left (top) to right (bottom) according to condensin and cohesin enrichment (Fig. 5e,f). Each group contains 122 bins. Contact scores were distance normalized as described above. Distance-normalized contact scores between 5-kb bins from the respective groups were used to calculate their averages. Average distance-normalized contact scores were separately estimated for the <75 kb and 75-kb–1-Mb distances. Binding strength scores ranging from 1 to 19 and average contact scores were subjected to the Pearson's correlation calculation.

Comparison between ChIA-PET and *in situ* Hi-C data

The *in situ* Hi-C data were compared to the Cut14 condensin and Rad21 cohesin ChIA-PET data[21]. 1,000 genomic interactions were randomly selected from the top 3.5% of condensin and 1% of cohesin ChIP-PET interactions. Genomic contacts with same distances were randomly selected (distance-conserved random sampling) from every combination. This sampling was repeated 10,000 times, and distributions of percent overlap with the large and small domains were plotted (Fig. 6c,f). For *P* value calculation, the same sampling was repeated 100 times, and distributions of percent-overlap scores were subjected to one-sided Student's *t* test.

Chromatin immunoprecipitation (ChIP)

ChIP was performed as previously described[52,53], with slight modifications. Chromatin was sheared using a Bioruptor (Diagenode). Tagged proteins were purified by mouse monoclonal anti-Pk (SV5-Pk1, Serotec) or mouse monoclonal anti-Myc (9E10, Clontech) and subsequently by protein G–coupled Dynabeads (Thermo Fisher Scientific). ChIP samples were analyzed using the 7900HT fast real-time PCR system (Thermo Fisher Scientific).

Microscopy

FISH experiments were performed as previously described[54,55]. To generate FISH probes, plasmid, cosmid, or PCR products were labeled by incorporation of Cy3-dCTP or Cy5-dCTP (GE Healthcare) with a random primer DNA labeling kit (Takara). The plasmid pRS140 and cosmid cos212 were used to prepare FISH probes against centromeres and telomeres, respectively[54,56]. FISH probes for other gene loci were generated using PCR-amplified DNA fragments (~15 kb).

IF experiments were performed as previously described[52,57]. Fixed cells were incubated with primary antibodies such as 1:10,000 diluted rabbit polyclonal anti-Myc (ab9106, Abcam) and 1:1,000 diluted mouse monoclonal anti-Pk (SV5-Pk1, Serotech). Cells were subsequently incubated with secondary antibodies such as 1:1,000 diluted Cy3-conjugated anti-mouse IgG (115-165-003, Jackson ImmunoResearch) and 1:1,000 diluted Alexa Flour 488-conjugated anti-rabbit IgG (A11034, Molecular Probes). FISH and IF images were captured using a Zeiss Axioimager Z1 fluorescence microscope with an oil immersion objective lens (Plan Apochromat, 100×, NA 1.4, Zeiss). The images were acquired at 0.2-μm intervals in the *z* axis controlled by Axiovision 4.6.3 software (Zeiss). More than 100 cells were analyzed for microscopic experiments.

RNA analysis

Total RNA was extracted from cells as previously described[47]. Total RNA sample (~5 μg) was treated with 10 U of RNase-free DNase I (Promega) at 37 °C for 40 min and then purified by phenol/chloroform extraction. Reverse transcription was carried out with the high-capacity cDNA reverse-transcription kit (Applied Biosystems), and cDNA was used as a template in subsequent PCR with gene-specific primers (Power SYBR green PCR master mix, Applied Biosystems). RT-PCR samples were analyzed by the 7900HT fast real-time PCR system (Life Technologies).

RNA sequencing

Total RNA (10 μg) was treated with 20 U of DNase I (Promega) at 37 °C for 40 min and then purified by phenol/chloroform extraction. Total RNA (5 μg) was subjected to mRNA purification using oligo d(T)25 beads (NEB #E7490S). cDNA was synthesized from purified RNA (10–40 ng) using NEBNext RNA library prep master mix set for Illumina (NEB #E6110S) and then purified using AMPure XP beads (Beckman Coulter, A63880). cDNA libraries were prepared using NEBNext ultra DNA library prep kit for Illumina (NEB #E7370S) with multiplex oligos (NEB #7500S).

The cDNA samples were sequenced on the Illumina HiSeq 2000 platform to obtain 76-bp single-end reads. Sequenced reads were mapped to the fission yeast reference genome (version ASM294v2.30) using the STAR program (v2.5.2) (ref. 58). htseq-count software (v0.6.1) was used to estimate read numbers assigned to exons, and the read numbers were normalized using the TMM method[59,60]. Differentially expressed genes between wild-type and *cut14-208* condensin mutant cells were identified with the edgeR package using the dispersion value of 0.029, which was estimated from the *cut3-477* and *cut14-208* condensin

mutant samples treated as biological replicas[61]. FDR < 0.05 was used as a threshold to define significantly up- or downregulated genes.

Data availability

High-throughput sequencing data and processed *in situ* Hi-C contact score matrices have been deposited in NCBI's Gene Expression Omnibus (GEO)[62] and are accessible through GEO accession number GSE93198. Source data for Figures 1f, 2d–f, 3b,c and 5d are available in Supplementary Data Sets 1–8. Other data and source codes are available upon reasonable request. A **Life Sciences Reporting Summary** for this article is available.

Supplementary Material

Refer to Web version on PubMed Central for supplementary material.

Acknowledgments

We would like to thank the Wistar Institute Genomics and Bioinformatics Facilities for high-throughput sequencing and genomic data analyses, the Wistar Imaging Facility for microscopic analysis, and the Yeast Genetic Resource Center (YGRC) for fission yeast strains. We also thank L. Showe and R. Locke for critically reading the manuscript and S. Shaffer for editorial assistance. This work was supported by the G. Harold & Leila Y. Mathers Charitable Foundation and by grants from the National Institutes of Health/National Institute of General Medical Sciences (R01GM124195 to K.N.) and the NIH Director's New Innovator Award Program (DP2-OD004348 to K.N.). Support for Shared Resources used in this study was provided by Cancer Center Support Grant (CCSG) P30CA010815 to the Wistar Institute.

References

1. Lieberman-Aiden E, et al. Comprehensive mapping of long-range interactions reveals folding principles of the human genome. Science. 2009; 326:289–293. [PubMed: 19815776]
2. Fullwood MJ, et al. An oestrogen-receptor-alpha-bound human chromatin interactome. Nature. 2009; 462:58–64. [PubMed: 19890323]
3. Dekker J, Misteli T. Long-range chromatin interactions. Cold Spring Harb Perspect Biol. 2015; 7:a019356. [PubMed: 26430217]
4. Phillips-Cremins JE, et al. Architectural protein subclasses shape 3D organization of genomes during lineage commitment. Cell. 2013; 153:1281–1295. [PubMed: 23706625]
5. Dowen JM, et al. Control of cell identity genes occurs in insulated neighborhoods in mammalian chromosomes. Cell. 2014; 159:374–387. [PubMed: 25303531]
6. Tang Z, et al. CTCF-mediated human 3D genome architecture reveals chromatin topology for transcription. Cell. 2015; 163:1611–1627. [PubMed: 26686651]
7. Dixon JR, et al. Topological domains in mammalian genomes identified by analysis of chromatin interactions. Nature. 2012; 485:376–380. [PubMed: 22495300]
8. Nora EP, et al. Spatial partitioning of the regulatory landscape of the X-inactivation centre. Nature. 2012; 485:381–385. [PubMed: 22495304]
9. Sexton T, et al. Three-dimensional folding and functional organization principles of the *Drosophila* genome. Cell. 2012; 148:458–472. [PubMed: 22265598]
10. Hou C, Li L, Qin ZS, Corces VG. Gene density, transcription, and insulators contribute to the partition of the *Drosophila* genome into physical domains. Mol Cell. 2012; 48:471–484. [PubMed: 23041285]
11. Pope BD, et al. Topologically associating domains are stable units of replication-timing regulation. Nature. 2014; 515:402–405. [PubMed: 25409831]
12. Eser U, et al. Form and function of topologically associating genomic domains in budding yeast. Proc Natl Acad Sci USA. 2017; 114:E3061–E3070. [PubMed: 28348222]

13. Naumova N, et al. Organization of the mitotic chromosome. Science. 2013; 342:948–953. [PubMed: 24200812]
14. Dileep V, et al. Topologically associating domains and their long-range contacts are established during early G1 coincident with the establishment of the replication-timing program. Genome Res. 2015; 25:1104–1113. [PubMed: 25995270]
15. Nagano T, et al. Cell-cycle dynamics of chromosomal organization at single-cell resolution. Nature. 2017; 547:61–67. [PubMed: 28682332]
16. Nasmyth K, Haering CH. The structure and function of SMC and kleisin complexes. Annu Rev Biochem. 2005; 74:595–648. [PubMed: 15952899]
17. Koshland D, Strunnikov A. Mitotic chromosome condensation. Annu Rev Cell Dev Biol. 1996; 12:305–333. [PubMed: 8970729]
18. Hirano T. Chromosome cohesion, condensation, and separation. Annu Rev Biochem. 2000; 69:115–144. [PubMed: 10966455]
19. Bauer CR, Hartl TA, Bosco G. Condensin II promotes the formation of chromosome territories by inducing axial compaction of polyploid interphase chromosomes. PLoS Genet. 2012; 8:e1002873. [PubMed: 22956908]
20. Crane E, et al. Condensin-driven remodelling of X chromosome topology during dosage compensation. Nature. 2015; 523:240–244. [PubMed: 26030525]
21. Kim KD, Tanizawa H, Iwasaki O, Noma K. Transcription factors mediate condensin recruitment and global chromosomal organization in fission yeast. Nat Genet. 2016; 48:1242–1252. [PubMed: 27548313]
22. Iwasaki O, Corcoran CJ, Noma K. Involvement of condensin-directed gene associations in the organization and regulation of chromosome territories during the cell cycle. Nucleic Acids Res. 2016; 44:3618–3628. [PubMed: 26704981]
23. Li L, et al. Widespread rearrangement of 3D chromatin organization underlies polycomb-mediated stress-induced silencing. Mol Cell. 2015; 58:216–231. [PubMed: 25818644]
24. Ji X, et al. 3D chromosome regulatory landscape of human pluripotent cells. Cell Stem Cell. 2016; 18:262–275. [PubMed: 26686465]
25. Rao SSP, et al. A 3D map of the human genome at kilobase resolution reveals principles of chromatin looping. Cell. 2014; 159:1665–1680. [PubMed: 25497547]
26. Belton JM, et al. Hi-C: a comprehensive technique to capture the conformation of genomes. Methods. 2012; 58:268–276. [PubMed: 22652625]
27. Mizuguchi T, et al. Cohesin-dependent globules and heterochromatin shape 3D genome architecture in *S. pombe*. Nature. 2014; 516:432–435. [PubMed: 25307058]
28. Takata H, et al. Proteome analysis of human nuclear insoluble fractions. Genes Cells. 2009; 14:975–990. [PubMed: 19695025]
29. Yokoyama Y, Zhu H, Zhang R, Noma K. A novel role for the condensin II complex in cellular senescence. Cell Cycle. 2015; 14:2160–2170. [PubMed: 26017022]
30. Bystricky K, Laroche T, van Houwe G, Blaszczyk M, Gasser SM. Chromosome looping in yeast: telomere pairing and coordinated movement reflect anchoring efficiency and territorial organization. J Cell Biol. 2005; 168:375–387. [PubMed: 15684028]
31. Berger AB, et al. High-resolution statistical mapping reveals gene territories in live yeast. Nat Methods. 2008; 5:1031–1037. [PubMed: 18978785]
32. Kim KD, et al. Centromeric motion facilitates the mobility of interphase genomic regions in fission yeast. J Cell Sci. 2013; 126:5271–5283. [PubMed: 23986481]
33. Sofueva S, et al. Cohesin-mediated interactions organize chromosomal domain architecture. EMBO J. 2013; 32:3119–3129. [PubMed: 24185899]
34. Zuin J, et al. Cohesin and CTCF differentially affect chromatin architecture and gene expression in human cells. Proc Natl Acad Sci USA. 2014; 111:996–1001. [PubMed: 24335803]
35. Kakui, Y., Rabinowitz, A., Barry, DJ., Uhlmann, F. Condensin-mediated remodeling of the mitotic chromatin landscape in fission yeast. Nat Genet. 2017. http://dx.doi.org/10.1038/ng.3938
36. Nasmyth K. Disseminating the genome: joining, resolving, and separating sister chromatids during mitosis and meiosis. Annu Rev Genet. 2001; 35:673–745. [PubMed: 11700297]

37. Sanborn AL, et al. Chromatin extrusion explains key features of loop and domain formation in wild-type and engineered genomes. Proc Natl Acad Sci USA. 2015; 112:E6456–E6465. [PubMed: 26499245]
38. Fudenberg G, et al. Formation of chromosomal domains by loop extrusion. Cell Rep. 2016; 15:2038–2049. [PubMed: 27210764]
39. Cheng TM, et al. A simple biophysical model emulates budding yeast chromosome condensation. eLife. 2015; 4:e05565. [PubMed: 25922992]
40. Hudson DF, Vagnarelli P, Gassmann R, Earnshaw WC. Condensin is required for nonhistone protein assembly and structural integrity of vertebrate mitotic chromosomes. Dev Cell. 2003; 5:323–336. [PubMed: 12919682]
41. Vagnarelli P, et al. Condensin and Repo-Man-PP1 co-operate in the regulation of chromosome architecture during mitosis. Nat Cell Biol. 2006; 8:1133–1142. [PubMed: 16998479]
42. Saka Y, et al. Fission yeast cut3 and cut14, members of a ubiquitous protein family, are required for chromosome condensation and segregation in mitosis. EMBO J. 1994; 13:4938–4952. [PubMed: 7957061]
43. Noma K. The yeast genomes in three dimensions: mechanisms and functions. Annu Rev Genet. 2017; 51:23–44. [PubMed: 28853923]
44. Yang, T., et al. HiCRep: assessing the reproducibility of Hi-C data using a stratum- adjusted correlation coefficient. 2017. http://dx.doi.org/10.1101/gr.220640.117
45. Gadaleta MC, Iwasaki O, Noguchi C, Noma K, Noguchi E. New vectors for epitope tagging and gene disruption in *Schizosaccharomyces pombe*. Biotechniques. 2013; 55:257–263. [PubMed: 24215641]
46. Bähler J, et al. Heterologous modules for efficient and versatile PCR-based gene targeting in *Schizosaccharomyces pombe*. Yeast. 1998; 14:943–951. [PubMed: 9717240]
47. Alfa, C., Fantes, P., Hyams, JS., McLeod, M., Wabrik, E. Experiments with Fission Yeast: A Laboratory Manual. Cold Spring Harbor Laboratory Press; 1993.
48. Langmead B, Trapnell C, Pop M, Salzberg SL. Ultrafast and memory-efficient alignment of short DNA sequences to the human genome. Genome Biol. 2009; 10:R25. [PubMed: 19261174]
49. Imakaev M, et al. Iterative correction of Hi-C data reveals hallmarks of chromosome organization. Nat Methods. 2012; 9:999–1003. [PubMed: 22941365]
50. Van Bortle K, et al. Insulator function and topological domain border strength scale with architectural protein occupancy. Genome Biol. 2014; 15:R82. [PubMed: 24981874]
51. Benjamini Y, Hochberg Y. Controlling the false discovery rate: a practical and powerful approach to multiple testing. J R Statist Soc B. 1995; 57:289–300.
52. Iwasaki O, Tanaka A, Tanizawa H, Grewal SIS, Noma K. Centromeric localization of dispersed Pol III genes in fission yeast. Mol Biol Cell. 2010; 21:254–265. [PubMed: 19910488]
53. Noma K, Allis CD, Grewal SI. Transitions in distinct histone H3 methylation patterns at the heterochromatin domain boundaries. Science. 2001; 293:1150–1155. [PubMed: 11498594]
54. Sadaie M, Naito T, Ishikawa F. Stable inheritance of telomere chromatin structure and function in the absence of telomeric repeats. Genes Dev. 2003; 17:2271–2282. [PubMed: 12952894]
55. Kim KD, Iwasaki O, Noma K. An IF–FISH approach to covisualization of gene loci and nuclear architecture in fission yeast. Methods Enzymol. 2016; 574:167–180. [PubMed: 27423862]
56. Chikashige Y, et al. Composite motifs and repeat symmetry in *S. pombe* centromeres: direct analysis by integration of NotI restriction sites. Cell. 1989; 57:739–751. [PubMed: 2541922]
57. Noma K, Grewal SIS. Histone H3 lysine 4 methylation is mediated by Set1 and promotes maintenance of active chromatin states in fission yeast. Proc Natl Acad Sci USA. 2002; 99(Suppl 4):16438–16445. [PubMed: 12193658]
58. Dobin A, et al. STAR: ultrafast universal RNA-seq aligner. Bioinformatics. 2013; 29:15–21. [PubMed: 23104886]
59. Anders S, Pyl PT, Huber W. HTSeq—a Python framework to work with high-throughput sequencing data. Bioinformatics. 2015; 31:166–169. [PubMed: 25260700]
60. Robinson MD, Oshlack A. A scaling normalization method for differential expression analysis of RNA-seq data. Genome Biol. 2010; 11:R25. [PubMed: 20196867]

61. Robinson MD, McCarthy DJ, Smyth GK. edgeR: a Bioconductor package for differential expression analysis of digital gene expression data. Bioinformatics. 2010; 26:139–140. [PubMed: 19910308]

62. Edgar R, Domrachev M, Lash AE. Gene Expression Omnibus: NCBI gene expression and hybridization array data repository. Nucleic Acids Res. 2002; 30:207–210. [PubMed: 11752295]

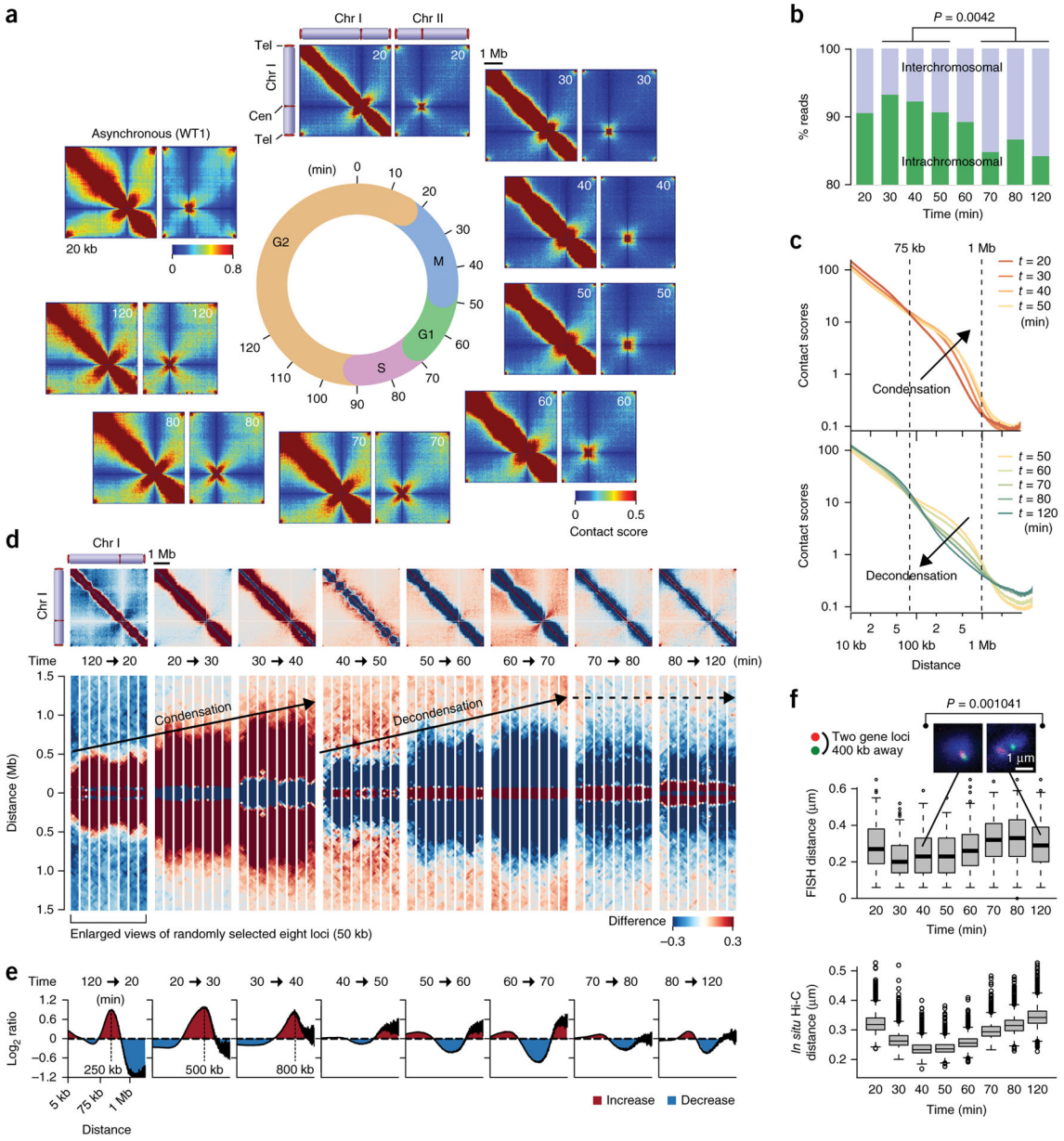

Figure 1.

Genomic architecture changes throughout the fission yeast cell cycle. (**a**) Intra- (chromosome I) and interchromosomal (chromosomes I and II) contact maps during the cell cycle. (**b**) Percentages of *in situ* Hi-C reads representing inter- and intrachromosomal contacts. Read numbers reflecting interchromosomal contacts during M phase (30-, 40-, and 50-min points) and during interphase (70-, 80-, and 120-min points) were subjected to two-sided Student's *t* test. (**c**) Relations between contact scores and genomic distances. Contact scores between gene loci separated by the same distances were used to calculate average scores, which were plotted against distance. (**d**) Difference of contact scores between two consecutive time points. Red and blue dots indicate that contact scores are increased and decreased, respectively, upon cell-cycle progression between the indicated time points.

Bottom panels show enlarged views of eight randomly selected loci (50 kb). (**e**) Average $\log_2$ ratios of contact scores between two consecutive time points. Average $\log_2$ ratios were calculated for every two loci separated by same distances and plotted against distance. (**f**) FISH analysis covisualizing the two gene loci during the cell cycle. The two loci are located 400 kb apart. Distance between two FISH foci was measured in more than 100 cells at the indicated time points. Representative images are shown on top (n = 108 and n = 132 for 40- and 120-min time points, respectively). Boxplots show center quartiles, midlines show medians and whiskers extend to the data points, which are no more than 1.5× the interquartile range from the box. Circles indicate outliers. Bottom, contact scores between every two loci located 400 kb apart were converted to physical distances using the conversion formula obtained by comparing contact scores and FISH data (Supplementary Fig. 2e). Physical distances estimated from contact scores were plotted as boxplots defined as above at the respective time points. Source data for **f** are available in Supplementary Data Sets 1 and 2.

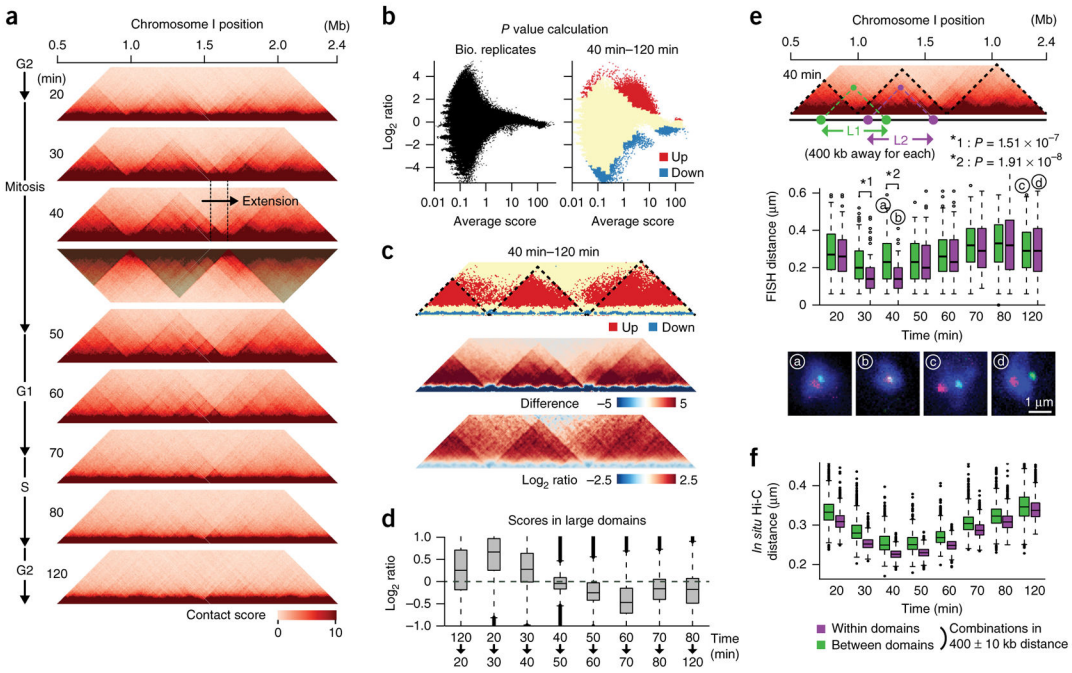

Figure 2.

Regulation of large domains during the cell cycle. (**a**) Contact maps for the 1.9-Mb area at the indicated time points. Domains (shaded) were defined at the 40-min time point as described in Supplementary Figure 6. (**b**) Detection of significantly altered contacts. Averages and $\log_2$ ratios of contact scores between two *in situ* Hi-C experiments using independent cell cultures (120-min point) and between the 40- and 120-min time points were plotted. Significantly upregulated (red) and downregulated (blue) genomic contacts were defined using the variation of contact scores between the biological replicates (Online Methods). (**c**) Significantly upregulated (red) and downregulated (blue) contacts were plotted along the same area as in **a** (top). Dotted lines indicate the large domains. Difference (middle) and $\log_2$ ratios (bottom) of contact scores between the 40- and 120-min time points were also plotted for the same area. (**d**) Log_2 ratios of contact scores between the indicated consecutive time points were calculated for all genomic contacts within the large domains and represented as boxplots. Source data for **d** are available in Supplementary Data Set 3. (**e**) FISH validation. The L1 and L2 paired gene loci located 400 kb apart were examined using FISH during the cell cycle. The distance between two FISH foci was measured in more than 100 cells during the cell cycle, and distances between the paired loci were plotted as boxplots at the indicated time points. Green and purple boxes indicate L1 and L2 data, respectively. Representative FISH images (denoted a–d) are shown below (n = 108, 103, 132 and 125 for a, b, c and d, respectively). Source data for L2 are available in Supplementary Data Set 1 and for L1 in Supplementary Data Set 4. (**f**) Every set of paired loci separated by 400 kb were divided to the two categories, in which they are located either within (purple) or between (green) the large domains. Contact scores from the two categories were converted to physical distances (see Fig. 1f), which were plotted as boxplots. Source data for **f** are available in Supplementary Data Set 5. All boxplot edges show center quartiles, midlines

show medians, and whiskers extend to the data points, which are no more than 1.5× the interquartile range from the box. Circles indicate outliers.

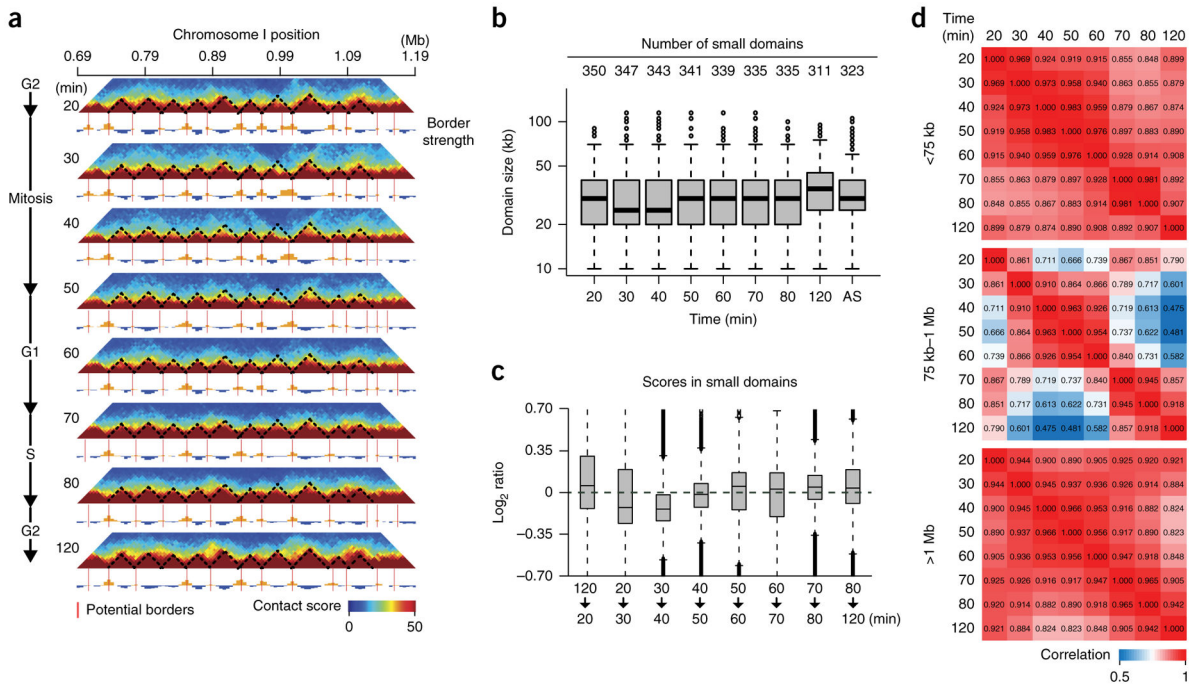

Figure 3.

Organization of small domains across the cell cycle. (**a**) Contact maps for the 500-kb genomic region during the cell cycle. Positive border strength scores were defined as borders (red lines). Dotted lines represent the conserved domains across the cell cycle. (**b**) Domain sizes during the cell cycle. Numbers of the predicted small domains are shown at top. Domain sizes are represented as boxplots. Source data for **b** are available in Supplementary Data Set 6. (**c**) Log_2 ratios of contact scores between the indicated consecutive time points were calculated for all genomic contacts within the small domains and represented as boxplots. Source data for **c** are available in Supplementary Data Set 7. (**d**) Correlations between contact maps were evaluated using the HiCRep program[44]. Note that genomic contacts were divided into three categories (<75 kb, 75 kb–1 Mb, and >1 Mb) on the basis of distances between two loci and that correlations were calculated for the respective categories. For **b** and **c**, all boxplot edges show center quartiles, midlines show medians, and whiskers extend to the data points, which are no more than 1.5× the interquartile range from the box. Circles indicate outliers.

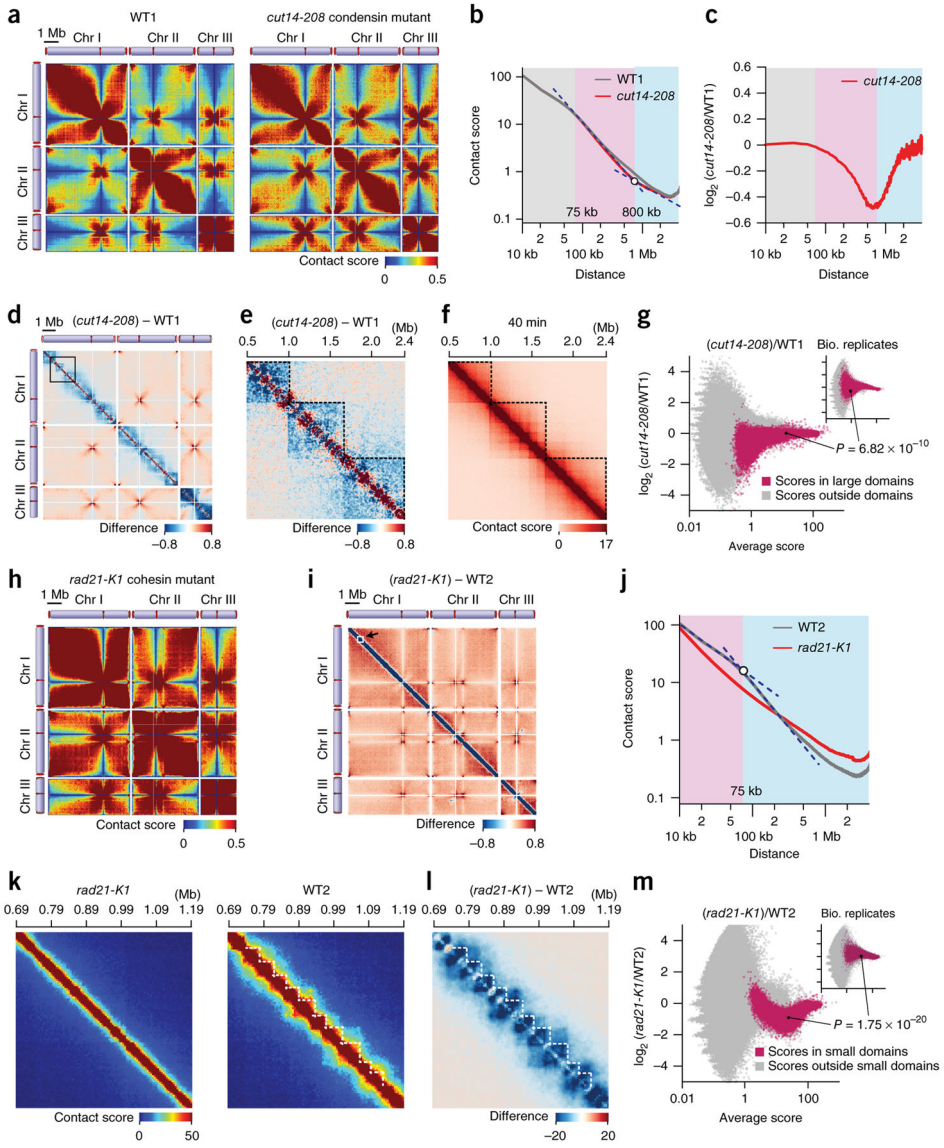

Figure 4.

Effects of condensin and cohesin mutations on domain organizations. (**a**) Contact maps in the wild-type (WT1) and *cut14-208* condensin mutant. (**b**) Relations between contact scores and genomic distances in WT1 and *cut14-208* cells. Dotted lines show the fitting lines against the slopes in the 75–800-kb and >800-kb ranges. (**c**) Log_2 ratios of contact scores between *cut14-208* and WT1 cells plotted against distance. (**d**) Map showing difference of contact scores between *cut14-208* and WT1. (**e**) Enlarged difference map for the 1.9-Mb area indicated by the open box in **d**. Dotted lines indicate the large domains. (**f**) Enlarged contact map at the 40-min time point. (**g**) Averages and log_2 ratios of contact scores between the *cut14-208* mutant and WT1 and between two *in situ* Hi-C experiments using independent cell cultures (120-min point; inset). Genomic contacts within the large domains (red) were separated from other contacts (gray) and were used in the analysis. 100 combinations of genomic loci were randomly selected from the large domains. Log_2 ratios

of contact scores between the *cut14-208* mutant and WT1 and between the biological replicates (120-min point) were extracted for the selected 100 combinations and subjected to two-sided paired Student's *t* test. Random sampling was repeated 1,000 times and a median of *P* values is represented. (**h**) A contact map in the *rad21-K1* cohesin mutant. (**i**) A map showing difference of contact scores between the *rad21-K1* mutant and WT2. (**j**) Relations between contact scores and genomic distances in the WT2 and *rad21-K1* mutant. Dotted lines show the fitting lines against the slopes in the <75-kb and >75-kb ranges. (**k**) Contact maps for the 500-kb region indicated by the open box in **i** in *rad21-K1* (left) and WT2 cells (right). Dotted lines indicate the small domains. (**l**) Enlarged difference map between the *rad21-K1* and WT2 for the same 500 kb-region. (**m**) Averages and $\log_2$ ratios of contact scores between the *rad21-K1* mutant and WT2 and between two *in situ* Hi-C experiments using independent cell cultures (120-min point; inset). The *rad21-K1* and WT2 small domains were subjected to the same statistical analyses as described in **g**.

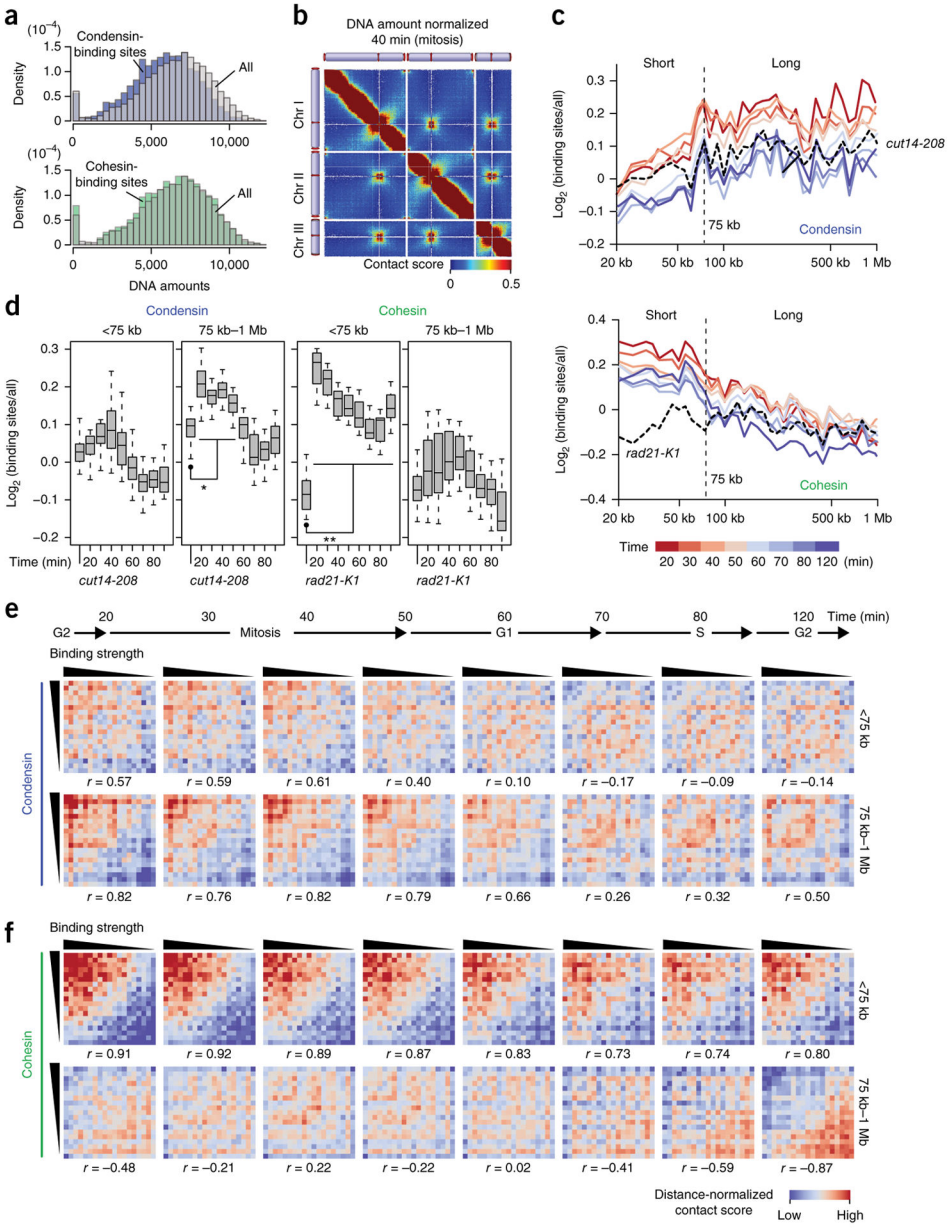

Figure 5.

Condensin- and cohesin-binding sites mediate long- and short-range contacts, respectively. (**a**) The DNA amounts of condensin-binding sites (n = 485; top) and cohesin-binding sites (n = 475; bottom) were compared to the distribution of every locus[21]. DNA amounts of respective gene loci were estimated based on the distribution of sequenced reads derived from self-ligation and undigested products (Online Methods). (**b**) A contact map after DNA-amount normalization (Online Methods). (**c**) The *in situ* Hi-C data from the different cell-cycle stages and *cut14-208* condensin mutant were subjected to DNA-amount normalization. Average contact scores between condensin-binding sites (5-kb bins) separated by same distances were divided by distance-conserved average contact scores estimated from every bin. Their $\log_2$ ratios were plotted against distance (top). The same analysis was performed

for cohesin-binding sites and with the *rad21-K1* cohesin mutant (bottom). (**d**) Distributions of $\log_2$ scores in **c** are separately summarized for the <75-kb and 75 kb–1 Mb distances. *P* values were calculated using two-sided paired Student's *t* test ($n = 13$ and 26 for <75 kb and 75 kb–1 Mb, respectively). Asterisk (*) indicates that $\log_2$ scores at each time point were significantly different from those of the *cut14-208* (*P* values = 2.20×10^{-5} (20 min), 5.09×10^{-7} (30 min), 8.70×10^{-6} (40 min)). Double asterisk (**) indicates that $\log_2$ scores across the cell cycle were significantly different from those of the *rad21-K1* (*P* values = 7.82×10^{-5} (20 min), 0.000153 (30 min), 0.000182 (40 min), 0.000193 (50 min), 0.000560 (60 min), 0.00119 (70 min), 0.00161 (80 min), 0.000953 (120 min)). Boxplot edges show center quartiles, midlines show medians, and whiskers extend to the data points, which are no more than 1.5× the interquartile range from the box. Source data for **d** are available in Supplementary Data Set 8. (**e**) Condensin binding strength versus distance-dependent contacts. Binding strength and distance-normalized contact scores were subjected to the Pearson's correlation (*r*) calculation (Online Methods). (**f**) Cohesin binding strength versus distance-dependent contacts, subjected to same statistical analyses as described in **e**.

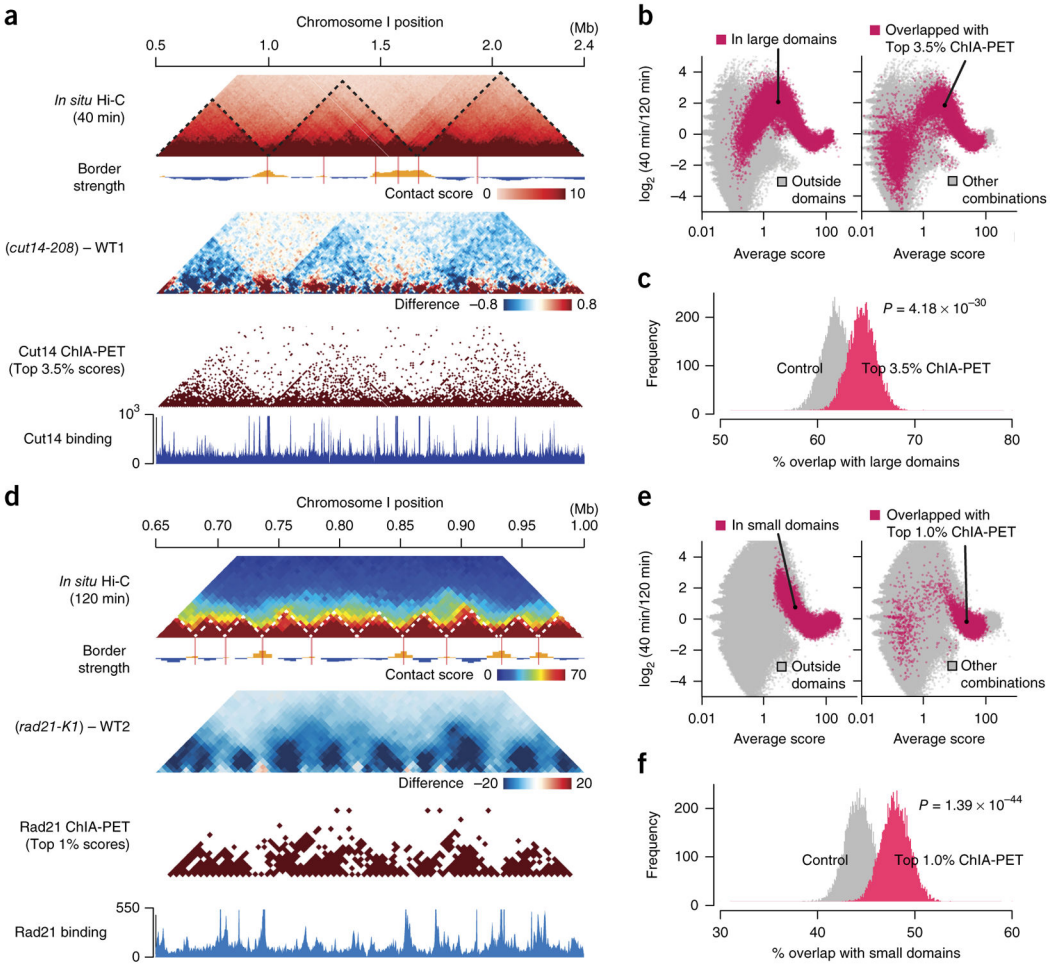

Figure 6.

Comparison between the *in situ* Hi-C and ChIA-PET data (**a**) *In situ* Hi-C data were compared to the Cut14 condensin ChIA-PET data[21]. Maps for the 1.9-Mb region show contact scores at the 40-min time point (mid M; top) and difference of contact scores between the *cut14-208* mutant and WT1 (second). The ChIA-PET data were analyzed using the same procedure applied to the *in situ* Hi-C data (Supplementary Fig. 1b). The top 3.5% of condensin-mediated contacts were extracted from the ChIA-PET data and plotted (third). Based on the ChIA-PET data, condensin enrichment and binding sites were predicted (bottom) as described in ref. 21. (**b**) Averages and $\log_2$ ratios of contact scores between the 40- and 120-min points were plotted for genomic contacts within (red) and outside (gray) the large domains (left). The same data were annotated differently for genomic contacts that overlapped with the top 3.5% condensin-mediated contacts (red) and others (gray) (right). (**c**) The top 3.5% of condensin-mediated contacts predicted from the ChIA-PET data were frequently positioned within the large domains (Online Methods). 1,000 genomic contacts were randomly selected from the top 3.5% of condensin ChIP-PET combinations. Genomic contacts with the same distances were randomly selected for distance-conserved random sampling from every combination. This sampling was repeated 10,000 times, and distributions of % overlap with the large domains were plotted. For *P* value calculation, the

same sampling was repeated 100 times, and distributions of % overlap scores were subjected to one-sided Student's *t* test. (**d**) The *in situ* Hi-C data were compared to the Rad21 cohesin ChIA-PET data[21]. Based on the ChIA-PET data, cohesin enrichment and binding sites were predicted (bottom) as described in ref. 21. (**e**) Averages and $\log_2$ ratios of contact scores between the 40- and 120-min time points were plotted for genomic contacts within (red) and outside (gray) the small domains (left). The same data were differently annotated for genomic contacts that overlapped with the top 1% of cohesin-mediated contacts (red) and others (gray) (right). (**f**) The top 1% of cohesin-mediated contacts predicted from the ChIA-PET data were often located within the small domains. The same analysis as described in **c** was performed for the cohesin-mediated contacts and the small domains.

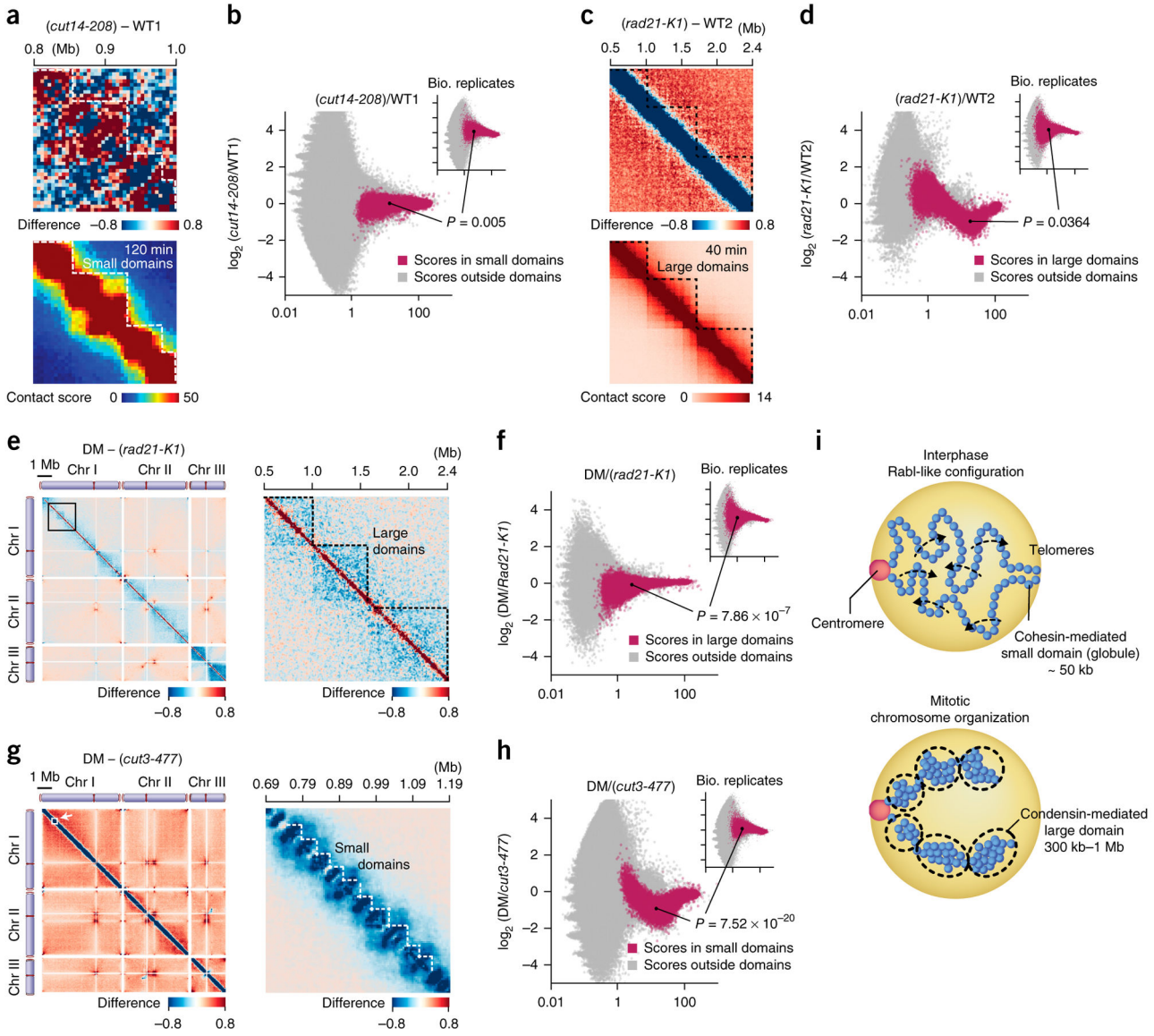

Figure 7.

Independence between condensin- and cohesin-mediated domain organizations. (**a**) Difference of contact scores between the *cut14-208* mutant and WT1 (top). The bottom panel represents the 120-min contact map. (**b**) Averages and $\log_2$ ratios of contact scores between the *cut14-208* mutant and WT1 and between two *in situ* Hi-C experiments using independent cell cultures (120-min point; inset) were plotted. Genomic contacts within the small domains (red) were separated from other contacts (gray) and were used in the analysis. 100 combinations of genomic loci were randomly selected from the small domains. Log_2 ratios of contact scores between the *cut14-208* mutant and WT1 and between the biological replicas (120-min point) were extracted for the selected 100 combinations and subjected to two-sided paired Student's *t* test. Random sampling was repeated 1,000 times and a median of *P* values is shown. (**c**) Difference of contact scores between the *rad21-K1* mutant and WT2 (top). The bottom panel represents the 40-min contact map. (**d**) Averages and $\log_2$

ratios of contact scores between the *rad21-K1* mutant and WT2 and between two *in situ* Hi-C experiments using independent cell cultures (120-min point; inset) were plotted. The same analysis described in **b** was performed with the *rad21-K1* for the large domains. (**e**) Left, difference of contact scores between the *cut3-477 rad21-K1* condensin–cohesin double mutant (DM) and the *rad21-K1* single mutant. Right, enlargement of the genomic region marked by the open box in left panel. (**f**) Averages and $\log_2$ ratios of contact scores between the DM and *rad21-K1* mutant and between two *in situ* Hi-C experiments using independent cell cultures (120-min point; inset) were plotted. The same analysis described in **b** was performed with the DM and *rad21-K1* for the large domains. (**g**) Left, difference of contact scores between the DM and *cut3-477* condensin single mutant. Right, enlargement of the genomic region indicated by the open box in left panel. (**h**) Averages and $\log_2$ ratios of contact scores between the DM and *cut3-477* mutant and between two *in situ* Hi-C experiments using independent cell cultures (120-min point; inset) were plotted. The same analysis as described in **b** was performed with the DM and *cut3-477* for the small domains. (**i**) A model explaining how the condensin- and cohesin-mediated contact domains are regulated during the cell cycle (see Discussion for details).